

Element Diffusion During Cosmological Structure Formation

David Medvigy & Abraham Loeb

Harvard-Smithsonian Center for Astrophysics, 60 Garden St., Cambridge, MA 02138;
dmedvigy@cfa.harvard.edu, aloeb@cfa.harvard.edu

ABSTRACT

We consider element diffusion during the linear growth of structure in the intergalactic medium (IGM) before the redshift of reionization. The elements produced during big bang nucleosynthesis (such as D, ^4He or ^7Li) condensed in collapsing regions more readily than hydrogen. Diffusion was most effective when the IGM was neutral since the collisional cross-section between neutral species is smaller than the corresponding Coulomb cross-section in an ionized gas. We find that diffusion led to small deviations in element abundances of up to 0.1%. Abundance measurements to this level of precision in low-metallicity environments could provide information about the thermal and ionization history of the primordial gas during the early formation of structure in the IGM.

Subject headings: cosmological parameters — cosmology: theory — diffusion — galaxies: abundances

1. Introduction

Recent attempts to measure the primordial ^4He abundance report accuracies better than $\sim 1\%$ (Izotov & Thuan 1998; Olive, Steigman, & Skillman 1997; Peimbert, Peimbert, & Ruiz 2000). Such accurate measurements are useful for testing the consistency of big bang nucleosynthesis and also for estimating the mean baryon density, Ω_b (Schramm & Turner 1998). The primordial ^4He mass fraction, \bar{Y} , is often inferred from the emission lines of blue compact galaxies (e.g., Peimbert & Torres-Peimbert 1974; Pagel, Terlevich, & Melnick 1986) under the implicit assumption that it had the same initial value throughout the Universe, including within underdense regions of the intergalactic medium (IGM).

However, a net difference between the element abundances in overdense and underdense regions could arise if diffusion occurs during the gravitational collapse of massive objects. Different atomic species, because of their different masses, will have different thermal speeds and will therefore experience different pressure forces per unit mass. Consequently, different elements would not flow into an overdense region at the same rate; instead, heavier elements would obtain higher relative abundances in galaxies than in voids. Diffusion is generally moderated by a frictional force

arising from inter-species collisions. These collisions are most frequent for an ionized gas (Spitzer 1956) in which the characteristic cross-section for ion-proton collisions, $\sim \pi(Ze^2/k_B T)^2 \ln \Lambda_C \sim 2 \times 10^{-12} Z(T/10^4 \text{ K})^{-2} \text{ cm}^2$, is far greater than the collision cross-section for the corresponding atoms in a neutral gas, $\sim 10^{-15} \text{ cm}^2$ (here, Ze is the ion charge, T is the temperature, k_B is Boltzmann’s constant, and $\ln \Lambda_C \sim 20$ is the Coulomb Logarithm). We therefore focus our attention on the period between cosmological recombination and reionization during which the IGM was neutral (Loeb & Barkana 2001). During this stage, atomic collision cross sections may be small enough to allow some diffusion to occur.

In this paper we quantify the diffusion of ^4He , ^7Li , and D relative to ^1H that occurs as a spherical, slightly overdense region begins to collapse. We assume a ΛCDM cosmology, characterized by densities relative to critical of $\Omega_m = 0.3$, $\Omega_\Lambda = 1 - \Omega_m$, and $\Omega_b = 0.045$ for matter, vacuum, and baryons; a Hubble constant of $H_0 = 70 \text{ km s}^{-1} \text{ Mpc}^{-1}$; a ^4He primordial mass fraction of $\bar{Y} = 0.244$; and primordial ^7Li and D number densities relative to ^1H of $\bar{X}_L = 1.75 \times 10^{-10}$ and $\bar{X}_D = 2.0 \times 10^{-5}$, respectively. The effects of diffusion are most important where the gas pressure matters, namely around the comoving Jeans length scale $\lambda_J = (2\pi/k_J)$. For redshifts $z \lesssim 140$, when the baryonic temperature is primarily determined by the adiabatic expansion, the Jeans wavenumber is (Barkana & Loeb 2001)

$$k_J = \left[\frac{0.9(1+z)\mu m_H \Omega_m H_0^2}{k_B T(z)} \right]^{1/2} \quad (1)$$

where $h = (H_0/100 \text{ km s}^{-1} \text{ Mpc}^{-1})$, μ is the mean molecular weight, m_H is the mass of hydrogen and $T(z)$ the baryonic temperature at a redshift z .

In § 2, we derive the differential equations used for our analysis. These are linearized equations which are strictly valid only as long as the overdensities remain small. However, we assume that reionization occurs before the collapsing region becomes significantly nonlinear and we stop our calculation at reionization because charged particle cross sections suppress any further diffusion. In § 3, we discuss the initial conditions used for our differential equations. In § 4, we compute both the mean abundance deviation and the typical abundance fluctuation within a collapsing region. We then use a Press-Schechter mass function to average the resulting deviations over all collapsed objects in the Universe. In § 5, we compare our model to recent measurements of ^4He abundances. Finally, we present our conclusions in § 6.

2. Basic Equations

We first establish our notation and illustrate our assumptions by carrying out a brief derivation of the equations satisfied by density perturbations. Each particle species has a mass density, ρ_s , and a bulk velocity, \mathbf{v}_s , which are related by the continuity equation,

$$\frac{\partial \rho_s}{\partial t} + \nabla_p \cdot (\rho_s \mathbf{v}_s) = 0, \quad (2)$$

where we start by using physical (proper) coordinates. Since the Universe is initially homogeneous, $\rho_s = \bar{\rho}_s(t)$ and all particles move with the Hubble flow: $\mathbf{v}_s = \bar{H}(t)\mathbf{x}$ (Peebles 1993). In this approximation, equation (2) becomes

$$\frac{\partial \bar{\rho}_s}{\partial t} + 3\bar{\rho}_s \bar{H} = 0. \quad (3)$$

We next allow for density and velocity perturbations through the definitions

$$\rho_s(\mathbf{x}, t) = \bar{\rho}_s(t) [1 + \delta_s(\mathbf{x}, t)], \quad (4)$$

$$\partial^i v_s^j(\mathbf{x}, t) = \sigma_s^{ij}(\mathbf{x}, t) + \omega_s^{ij}(\mathbf{x}, t) + [\bar{H}(t) + \delta H_s(\mathbf{x}, t)] \delta_{kron}^{ij}. \quad (5)$$

The velocity gradient is decomposed into a symmetric, traceless tensor (σ_s^{ij}), an antisymmetric tensor (ω_s^{ij}), and a trace. We insert these definitions into equation (2) and linearize the perturbations to obtain

$$\frac{\partial \delta_s}{\partial t} + (\mathbf{v}_s \cdot \nabla) \delta_s + 3\delta H_s = 0. \quad (6)$$

Switching from now on from physical to comoving coordinates, and letting an overdot represent a time derivative, equation (6) may be compactly expressed as

$$\dot{\delta}_s = -3\delta H_s. \quad (7)$$

The density and bulk velocity also satisfy a force equation; in comoving coordinates,

$$\dot{\mathbf{v}}_s = \rho_s^{-1} \sum_{forces} \mathbf{F}_s. \quad (8)$$

The sum on the right-hand side includes all forces acting on species s . We linearize this equation and make use of equation (7) to obtain a new equation which does not explicitly contain the velocity perturbations,

$$\ddot{\delta}_s + 2\bar{H}\dot{\delta}_s - 3\frac{\partial \bar{H}}{\partial t} - 3\bar{H}^2 = -\nabla \cdot \left[\frac{1}{\rho_s} \sum_{forces} \mathbf{F}_s \right]. \quad (9)$$

We now switch independent variables from time to redshift via the Friedmann equation, which leads to

$$H_0 t = \frac{2}{3\sqrt{\Omega_\Lambda}} \sinh^{-1} \left(\sqrt{\frac{\Omega_\Lambda}{\Omega_m}} (1+z)^{-3/2} \right). \quad (10)$$

However $\Omega_\Lambda = 0.7$ only becomes significant for $z \lesssim 1$; in this paper we consider redshifts $z \gg 1$ for which

$$H_0 t \approx \frac{2}{3\sqrt{\Omega_m}} (1+z)^{-3/2}. \quad (11)$$

Denoting a derivative with respect to z by a prime, equation (9) becomes

$$\delta_s'' + \frac{1}{2(1+z)} \delta_s' - \frac{3}{\Omega_m H_0^2 (1+z)^5} \left(\frac{\partial \bar{H}}{\partial t} + \bar{H}^2 \right) = -\frac{1}{\Omega_m H_0^2 (1+z)^5} \nabla \cdot \left[\frac{1}{\rho_s} \sum_{forces} \mathbf{F}_s \right]. \quad (12)$$

We now obtain expressions for the forces. The force due to gravity, when expressed in terms of the potential, ϕ , is $\mathbf{F}_s = -\rho_s \nabla \phi$. We insert this into equation (12) and use Poisson's equation which gives

$$\delta_s'' + \frac{1}{2(1+z)} \delta_s' = -\frac{1}{\Omega_m H_0^2 (1+z)^5} \nabla \cdot \left[\frac{1}{\rho_s} \sum'_{forces} \mathbf{F}_s \right] + \frac{3}{2\Omega_m} (1+z)^{-2} \sum_{species} \Omega_i \delta_i, \quad (13)$$

where the primed sum means a sum over all forces except gravity.

Although all types of particles are affected by gravity, we assume that only the baryons ever obtain a non-zero temperature. Each species of baryons experiences a different pressure force which is determined by the negative of its pressure gradient,

$$\mathbf{F}_s = -\nabla P_s = -\frac{k_B}{m_s} (\rho_s \nabla T_s + T_s \nabla \rho_s), \quad (14)$$

where we have used m_s for the atomic mass and T_s for the temperature of species s . Dividing equation (14) by the mass density and taking the divergence, we see that

$$\nabla \cdot \frac{\mathbf{F}_s}{\rho_s} = -\frac{k_B}{m_s} (\nabla^2 T_s + T_s \nabla^2 \delta_s) \quad (15)$$

to first order in the perturbations. We define \bar{T}_s to be the temperature in the absence of perturbations, and express the effects of perturbations in terms of the small quantity τ_s : $T_s = \bar{T}_s (1 + \tau_s)$. Inserting this into equation (15) and linearizing once more we see that

$$\nabla \cdot \frac{\mathbf{F}_s}{\rho_s} = -\frac{k_B \bar{T}_s}{m_s} (\nabla^2 \tau_s + \nabla^2 \delta_s). \quad (16)$$

The temperature of the baryons is determined by two effects, the coupling of free electrons to the background radiation and the adiabatic expansion (Peebles 1993). This gives

$$\frac{dT_s}{dt} = \frac{x}{1+x} \frac{8\sigma_T a T_\gamma^4}{3m_e c} (T_\gamma - T_s) + \frac{2T_s}{3\rho_s} \frac{d\rho_s}{dt}, \quad (17)$$

where x is the free electron fraction, σ_T is the Thomson cross section, a is the Stefan-Boltzmann constant, m_e is the electron mass, c is the speed of light, and T_γ is the temperature of the cosmic microwave background (CMB). Switching the independent variable to z and linearizing, equation (17) becomes

$$\frac{dT_s}{dz} = -\frac{x}{1+x} \frac{8\sigma_T a T_0^5 (1+z)^{5/2}}{3m_e c H_0 \sqrt{\Omega_m}} \left(1 - \frac{T_s}{T_0 (1+z)} \right) + \frac{2T_s}{(1+z)} + \frac{2}{3} T_s \delta_s', \quad (18)$$

where $T_0 = 2.73$ K is the CMB temperature at present.

The mean baryon temperature, \bar{T}_s , is defined to be a solution of

$$\frac{d\bar{T}_s}{dz} = -\frac{x}{1+x} \frac{8\sigma_T a T_0^5 (1+z)^{5/2}}{3m_e c H_0 \sqrt{\Omega_m}} \left(1 - \frac{\bar{T}_s}{T_0 (1+z)} \right) + \frac{2\bar{T}_s}{(1+z)}. \quad (19)$$

This indicates that \bar{T}_s is independent of baryonic species and so all baryons would be at the same temperature in the absence of perturbations. We use the computer program RECFAST (Seager, Sasselov, & Scott 1999) to determine the free-electron fraction as a function of redshift. Then we use equation (19) to compute the mean baryon temperature. Both quantities are shown in Figure 1.

After linearizing equation (18), we obtain the equations for the temperature perturbations,

$$w'_s - \frac{x}{1+x} \frac{8\sigma_T a T_0^5 (1+z)^{5/2}}{3m_e c H_0 \sqrt{\Omega_m}} \frac{w_s}{\bar{T}_s} = \frac{x}{1+x} \frac{16\sigma_T a T_0^5 (1+z)^{5/2}}{9m_e c H_0 \sqrt{\Omega_m}} \frac{\delta_s}{\bar{T}_s}, \quad (20)$$

where $w_s = \tau_s - \frac{2}{3}\delta_s$. With this definition of w_s , equation (16) becomes

$$\nabla \cdot \frac{\mathbf{F}_s}{\rho_s} = -\frac{k_B \bar{T}}{m_s} \left(\frac{5}{3} \nabla^2 \delta_s + \nabla^2 w_s \right). \quad (21)$$

Because of the spatial derivatives, we are forced to work in comoving Fourier space. However, for simplicity of notation we will continue to simply write δ_s and w_s , although from now on we use these symbols to represent the Fourier components of the perturbations.

Finally we take into account the frictional term arising from inter-species collisions. Physically, this force is non-zero only if two species have different bulk velocities; thus, the force on one species due to a second species may be written as $\mathbf{F}_1 = \kappa(\mathbf{x}, t)(\mathbf{v}_2 - \mathbf{v}_1)$ (Burgers 1969). Since the difference in bulk velocities is already linear in the perturbations, we only need to calculate the coefficient κ to zeroth order for the linearized equations of motion. This allows us to calculate κ under the assumption that all baryons share the same temperature. In general, the frictional force per unit volume acting on species i due to species j is obtained by multiplying the number of collisions per unit time per unit volume by the momentum transfer per collision. We multiply this by the probability that species i and j have initial momentum \mathbf{p}_i and \mathbf{p}_j and that the center of mass scattering angle is χ . Finally, we integrate over all parameters,

$$\mathbf{F}_{ij} = \int d^3\mathbf{p}_i \int d^3\mathbf{p}_j \int d\Omega n_i n_j \sigma_{ij} |\mathbf{v}_i - \mathbf{v}_j| \Delta\mathbf{p}_i(\mathbf{p}_i, \mathbf{p}_j, \chi) f_i(\mathbf{p}_i) f_j(\mathbf{p}_j) \frac{1}{\sigma_{ij}} \frac{d\sigma_{ij}}{d\Omega}(\mathbf{p}_i, \mathbf{p}_j, \chi). \quad (22)$$

We assume that the collisions are elastic and that the atoms can be approximated by hard spheres. We take each species to have a Maxwellian velocity distribution. Following the integration equation (22) becomes

$$\mathbf{F}_{ij} = -\frac{16m_{ij}}{3\sqrt{2\pi}} \sqrt{\frac{k_B \bar{T}}{m_{ij}}} n_i n_j \sigma_{cl} (\mathbf{v}_i - \mathbf{v}_j) \int_0^\infty dx x^5 e^{-x^2} Q_d \left(x \sqrt{\frac{k_B \bar{T}}{m_{ij}}} \right). \quad (23)$$

Here, $m_{ij} = m_i m_j / (m_i + m_j)$ is the reduced mass, σ_{cl} is the classical hard-sphere cross section, $n_i = \rho_i / m_i$, and the integral is a quantum mechanical correction (Massey, Burhop, & Gilbody 1969). The function $Q_d(q)$ is given by

$$Q_d = \frac{1}{q^2} \sum_{l=0}^{\infty} \left[4(2l+1) \sin^2 \eta_l - 2(l+1)(1 - \cos 2\eta_l - \cos 2\eta_{l+1} + \cos 2(\eta_l - \eta_{l+1})) \right]. \quad (24)$$

The integration variable x is related to q by $q = xa\sqrt{2m_{ij}k_B\bar{T}/\hbar^2}$, and the phase shifts are given by $\eta_0 = -q$ and $\tan \eta_i = (-1)^{i-1} J_{i+1/2}(q)/J_{-i-1/2}(q)$, where the functions $J_n(q)$ are Bessel functions of order n . The distance scale a represents the sum of the radii of two colliding atoms; we adopt the values $r_H = r_D = 0.53\text{\AA}$, $r_{He} = 0.31\text{\AA}$, and $r_{Li} = 1.45\text{\AA}$ (Clementi, Raimondi, & Reinhardt 1963; Slater 1964). We evaluate the integral in equation (23) numerically and plot the results in Figure 2 for each type of inter-species collision. Quantum mechanics becomes more important as the temperature decreases but the correction is never greater than a factor of four. For brevity, we henceforth denote this integral by $I_{ij}(z)$.

We now summarize the equations governing each species. For dark matter equation (12) becomes

$$\delta''_{dm} + \frac{1}{2}(1+z)^{-1}\delta'_{dm} = \frac{3}{2}(1+z)^{-2} \sum_{\text{species}} \frac{\Omega_i}{\Omega_m} \delta_i. \quad (25)$$

For each baryonic species there are also pressure and collisional friction terms, and so

$$\begin{aligned} \delta''_i + \frac{1}{2}(1+z)^{-1}\delta'_i &= \frac{3}{2}(1+z)^{-2} \sum_{j=\text{all species}} \frac{\Omega_j}{\Omega_m} \delta_j \\ &\quad - \frac{k_B\bar{T}}{m_i\Omega_m H_0^2} (1+z)^{-3} k^2 \left(\frac{5}{3}\delta_i + w_i \right) \\ &\quad + \frac{H_0}{G} \sqrt{\frac{2k_B\bar{T}}{\Omega_m\pi^3}} \sum_{j \neq i} \frac{\Omega_j \sigma_{cl}^{ij}}{\sqrt{m_i m_j (m_i + m_j)}} (1+z)^{1/2} I_{ij}(z) (\delta'_i - \delta'_j), \end{aligned} \quad (26)$$

where k is the comoving wave number. From equation (26) we can easily find the differential equations satisfied by the differences relative to hydrogen, $\Delta_i = \delta_i - \delta_H$:

$$\begin{aligned} \Delta''_i + \frac{1}{2}(1+z)^{-1}\Delta'_i &= \frac{k_B\bar{T}}{\Omega_m H_0^2} (1+z)^{-3} k^2 \left[\frac{5}{3} \left(\frac{\delta_H}{m_H} + \frac{\Delta_i - \delta_H}{m_i} \right) + \left(\frac{w_H}{m_H} - \frac{w_i}{m_i} \right) \right] \\ &\quad - \frac{H_0}{G} \sqrt{\frac{2k_B\bar{T}}{\Omega_m\pi^3}} \sum_{j \neq H} \frac{\Omega_j \sigma_{cl}^{H-j}}{\sqrt{m_H m_j (m_H + m_j)}} (1+z)^{1/2} I_{H-j}(z) \Delta'_j \\ &\quad + \frac{H_0}{G} \sqrt{\frac{2k_B\bar{T}}{\Omega_m\pi^3}} \sum_{j \neq i} \frac{\Omega_j \sigma_{cl}^{ij}}{\sqrt{m_i m_j (m_i + m_j)}} (1+z)^{1/2} I_{ij}(z) (\Delta'_j - \Delta'_i). \end{aligned} \quad (27)$$

3. Initial Conditions

We consider dark matter perturbations initially of the spherical top-hat form $\delta_{dm}(\mathbf{x}, z_{ini}) = \delta_{ini}\theta(R - |\mathbf{x}|)$, which has the Fourier components

$$\delta_{dm}(\mathbf{k}, z_{ini}) = \frac{4\pi\delta_{ini}}{k^3} (\sin kR - kR \cos kR). \quad (28)$$

Here, δ_{ini} and R are constants and θ represents the step function. We take the initial values of Δ_{He} , Δ_{Li} , Δ_D and their derivatives to be zero, but we would like to choose the initial values of

δ'_{dm} , δ_H , and δ'_H that correspond to the most rapidly growing mode. To gain some insight into how to make this choice, we consider a simplified problem where baryonic diffusion is negligible. We approximate the baryonic temperature by the temperature of the background radiation (valid for $z \gtrsim 200$; see Figure 1). Equation (26) for the baryon overdensity becomes

$$\delta''_b + \frac{1}{2}(1+z)^{-1}\delta'_b = \frac{3}{2}(1+z)^{-2}\left(\frac{\Omega_{dm}}{\Omega_m}\delta_{dm} + \frac{\Omega_b}{\Omega_m}\delta_b\right) - \frac{k_B T_0}{\mu\Omega_m H_0^2}(1+z)^{-2}k^2\delta_b. \quad (29)$$

We use this equation to express δ_{dm} , differentiate, and insert the results into equation (25). The outcome is a fourth order differential equation for δ_b . It has four independent, power law solutions which we write as $\delta_b = \sum_{i=1}^4 A_i (1+z)^{p_i}$. The four A_i are the four arbitrary constants associated with a linear fourth order equation. The four p_i are given by

$$p_i = \begin{cases} \frac{1}{4} + \sqrt{\frac{13}{16} - \frac{\hat{k}^2}{2} + \frac{1}{2}\sqrt{\left(\hat{k}^2 - \frac{3}{2}\right)^2 + 6\hat{k}^2\frac{\Omega_{dm}}{\Omega_m}}} \\ \frac{1}{4} + \sqrt{\frac{13}{16} - \frac{\hat{k}^2}{2} - \frac{1}{2}\sqrt{\left(\hat{k}^2 - \frac{3}{2}\right)^2 + 6\hat{k}^2\frac{\Omega_{dm}}{\Omega_m}}} \\ \frac{1}{4} - \sqrt{\frac{13}{16} - \frac{\hat{k}^2}{2} + \frac{1}{2}\sqrt{\left(\hat{k}^2 - \frac{3}{2}\right)^2 + 6\hat{k}^2\frac{\Omega_{dm}}{\Omega_m}}} \\ \frac{1}{4} - \sqrt{\frac{13}{16} - \frac{\hat{k}^2}{2} - \frac{1}{2}\sqrt{\left(\hat{k}^2 - \frac{3}{2}\right)^2 + 6\hat{k}^2\frac{\Omega_{dm}}{\Omega_m}}}, \end{cases} \quad (30)$$

where \hat{k}^2 is the squared comoving wavenumber normalized by $(\mu\Omega_m H_0^2/k_B T_0)$. The resulting expression for the dark matter overdensity is

$$\delta_{dm} = \sum_{i=1}^4 c_i A_i (1+z)^{p_i}, \quad (31)$$

with the constants c_i given by

$$c_i = p_i^2 \left(\frac{2\Omega_m}{3\Omega_{dm}}\right) - p_i \left(\frac{\Omega_m}{3\Omega_{dm}}\right) + \frac{2\hat{k}^2\Omega_m - 3\Omega_b}{3\Omega_{dm}}. \quad (32)$$

Motivated by this solution, we choose our initial conditions so that the perturbation will grow like the most negative p_i (i.e., the third one listed in equation 30). We let the three A_i corresponding to all but the largest growth rate be zero, and let the final A_i be determined by the tophat distribution (equation 28). The remaining initial conditions may now be written in terms of the known c_i and p_i .

4. Calculations

4.1. Evolution of the k -Modes

We define a new set of variables,

$$\hat{\delta}_s = \frac{k^3}{4\pi\delta_{ini}(\sin kR - kR \cos kR)}\delta_s, \quad (33)$$

$$\hat{\Delta}_s = \frac{k^3}{4\pi\delta_{ini}(\sin kR - kR \cos kR)}(\delta_s - \delta_H), \quad (34)$$

$$\hat{w}_s = \frac{k^3}{4\pi\delta_{ini}(\sin kR - kR \cos kR)}w_s. \quad (35)$$

These quantities are special because they not only satisfy the same differential equations as the δ and w , but also satisfy simpler initial conditions, $\hat{\delta}_{dm} = 1$, $\hat{\delta}'_{dm} = \frac{p_3}{1+z_{ini}}$, $\hat{\delta}_b = c_3^{-1}$, and $\hat{\delta}'_b = \frac{p_3}{c_3(1+z_{ini})}$. The parameters (δ_{ini}, R) have disappeared from the problem. Therefore we only evolve each normalized k -mode once; we obtain the physical overdensity for a given δ_{ini} and R by multiplying each k -mode by the appropriate factor from equation (33).

We have set $z_{ini} = 10^3$ following cosmological recombination. The final redshift is marked by the first of two possible events. Our equations are applicable in the linear regime, so we must stop if the object becomes nonlinear. At a transition to nonlinearity, the density would be greatly enhanced which would result in the suppression of diffusion. Therefore, we expect diffusion to be effective in the linear regime where our equations are valid. The second stopping condition relates to the reionization of the Universe. At that time, large Coulomb cross sections between charged particles are able to effectively halt diffusion. In conclusion, we consider the case where the object becomes nonlinear after reionization and adopt $z_{reion} = 8$ (Haiman & Loeb 1998, 1999a,b; Gnedin & Ostriker 1997; Chiu & Ostriker 2000; Gnedin 2000) as the stopping point of our diffusion calculation. Since the collapsed fraction of the Universe is small at $z = 8$ (Barkana & Loeb 2001), most of the material within galaxies that form much later (at $z \lesssim 3$) was still in the linear regime at $z \gtrsim 8$, where our diffusion calculation is adequate.

Several results of having carried out this prescription are shown in Figure 3. All length scales have been measured in terms of k_J^{-1} , defined in equation (1). This expression involves the baryonic temperature which is set by the adiabatic expansion for redshifts less than $z_t \approx 138$, $T(z) = T_0(1+z)^2(1+z_t)^{-1}$; as discussed in § 2. At z_{reion} , the Jeans wavenumber therefore obtains the value

$$k_J = 1040 \text{ Mpc}^{-1} \left[\left(\frac{9}{1+z} \right) \left(\frac{\Omega_m h^2}{0.147} \right) \left(\frac{2.73 \text{ K}}{T_0} \right) \right]^{1/2}, \quad (36)$$

which is the value used in Figure 3. We see that the dark matter overdensity has evolved approximately proportionally to $(1+z)^{-1}$, as might have been expected since gravity is the only force applicable to dark matter. On large scales corresponding to $k \lesssim k_J$, the baryons follow the dark matter; however, on small scales corresponding to $k \gtrsim k_J$, pressure forces prevent baryonic modes from collapsing. This leads to the slight decline in dark matter amplification near the Jeans scale

and the dramatic decline in the amplification of baryonic modes there. In the lower panel of Figure 3, we see that the perturbations of the different baryonic species do not experience exactly the same amplification. At $k \ll k_J$, pressure is negligible for all species, and the modes of each are amplified. Since hydrogen is the lightest species, it reaches its Jeans scale at the lowest k . Thus, all of the $\hat{\Delta}_x$ become positive at approximately the same wavenumber. As k increases, we begin to reach the Jeans scales of the heavier species. Then the growth of k -modes of this second species is also suppressed, and the $\hat{\Delta}_x$ approach zero as k gets large. However, Figure 3 indicates that the overall magnitude of diffusion is not solely determined by the Jeans scale of a species, or else the effect would have been largest for ${}^7\text{Li}$. This is because of the frictional term which serves to suppress diffusion, which is proportional to the square of the radius of an atom and therefore the greatest suppression is associated with the largest atoms.

The normalized overdensities in Figure 3 were obtained by evolving 1025 k -modes, equally spaced between with $0 \leq k/k_J \leq 100$. To obtain the physical overdensities, each mode must be multiplied by its normalization factor. The normalization factor depends on the object assembly radius R , and is fairly rapidly varying compared to the normalized overdensities. To get an accurate determination of the physical overdensity, we interpolate the normalized overdensity so that we sample it at a rate larger than the frequency of the normalization factor. We then use equation (33) to obtain the physical k -modes. One such sampling is shown in Figure 4. The value of R used for this plot corresponds to an enclosed mass of $M = 10^9 M_\odot = \rho_{\text{crit}} \Omega_m \frac{4}{3} \pi R^3$. The relative errors incurred in interpolation are typically $\sim 10^{-6}$, and seldom exceed 10^{-5} with the 1025 initial points. The normalization factor is also proportional to the initial dark matter perturbation, δ_{ini} , which we express in terms of the collapse redshift of the object (z_{coll}) through the approximate relation $\delta_{\text{ini}} (1 + z_{\text{ini}}) = \delta_{\text{coll}} (1 + z_{\text{coll}})$. We take $\delta_{\text{coll}} = 1.69$ for the overdensity of collapse and, unless otherwise stated, $z_{\text{coll}} = 2.5$ for the redshift of collapse. Such objects would be just on the fringe of nonlinearity at $z_{\text{reion}} = 8$. Since diffusion within all objects was shut off at z_{reion} , the effects of diffusion would be decreased for objects that collapsed later.

4.2. Predicted Statistics

4.2.1. Mean Abundances

Next we quantify the extent to which element abundances in collapsed objects differ from their primordial values. Abundances of ${}^4\text{He}$ are commonly reported in terms of the mass fraction,

$$Y = \frac{\bar{\rho}_{\text{He}} (1 + \delta_{\text{He}})}{\bar{\rho}_{\text{He}} (1 + \delta_{\text{He}}) + \bar{\rho}_{\text{H}} (1 + \delta_{\text{H}})}, \quad (37)$$

where we have neglected the contributions of all species but ${}^4\text{He}$ and ${}^1\text{H}$ to the mass of the Universe. After linearizing this equation, we see that

$$\frac{Y - \bar{Y}}{\bar{Y}} = (1 - \bar{Y}) (\delta_{\text{He}} - \delta_{\text{H}}). \quad (38)$$

In contrast, the abundances of ${}^7\text{Li}$ and D are typically reported in terms of their number densities relative to hydrogen. In this case,

$$\frac{X_{L,D} - \bar{X}_{L,D}}{\bar{X}_{L,D}} = (\delta_{Li,D} - \delta_H). \quad (39)$$

To see how the element abundances in collapsed objects differ, on average, from their primordial values, we average equations (38)- (39) over the original sphere of comoving radius R ,

$$\Delta_R = \frac{3}{4\pi R^3} \int_{\text{sphere}} d^3\mathbf{x} \int \frac{d^3\mathbf{k}}{(2\pi)^3} \Delta_{\mathbf{k}} e^{i\mathbf{k}\cdot\mathbf{x}}. \quad (40)$$

After integrating, we see that

$$\Delta_R = \frac{3}{2\pi^2 R^3} \int_0^\infty \frac{dk}{k} \Delta_k (\sin kR - kR \cos kR). \quad (41)$$

We carry out this final integration numerically. As described in § 4.1, we evolve 1025 k -modes between 0 and $100k_J$ to get the $\hat{\Delta}_x$ (where x could denote any of ${}^4\text{He}$, ${}^7\text{Li}$, D). We interpolate to get values for $\hat{\Delta}_x$ at a fixed number of points, and then multiply each point by its normalization. We then evaluate the integral in equation (41) with these points. Then we repeat the procedure, but with twice as many interpolated points. If the two results differ by less than a fraction of 5×10^{-3} , we stop and accept the result.

Figure 5 illustrates the dependence of these deviations on the size of the collapsed object. Instead of measuring the size of the object by its assembly radius, R , we instead measure it in terms of its mass defined by

$$M = \rho_{crit} \Omega_m \frac{4}{3} \pi R^3. \quad (42)$$

We see that the deviation from the primordial mean shrinks as the collapsed object increases in size approximately according to a power law with slope -0.33 . A simple argument yields the same result: assuming that the collapsing region starts out with primordial abundances throughout its volume and that diffusion occurs through the boundary of the region, the deviations from primordial abundances should fall off like $1/R$, or $M^{-1/3}$.

Now that element abundances for particular collapsed objects are known, we proceed by averaging these abundances over all objects in the Universe that have collapsed by a particular redshift. This statistic is approximated by using a Press-Schechter mass function; for ${}^4\text{He}$,

$$\langle Y \rangle = \frac{\int_{M_{min}}^\infty Y_M M \frac{dn}{dM} dM}{\int_{M_{min}}^\infty M \frac{dn}{dM} dM}, \quad (43)$$

where dn/dM is the number density of objects of mass M that have collapsed at a given redshift and Y_M is the averaged ${}^4\text{He}$ mass fraction within an object of mass M . Equation (43) is also appropriate for the ${}^7\text{Li}$ and D abundances if we replace Y with $X_{L,D}$. Note also that there is a

minimum mass scale of galaxies in which star formation is possible that we denote by M_{min} (Abel 1995; Tegmark et al. 1997). We use a code developed by Eisenstein & Hu (1999) and Barkana (2000) to calculate dn/dM at a redshift of 2.5. The averaged abundances differ from primordial by the amounts shown in Figure 6. We also consider a collapse redshift of $z_{coll} = 0$; in this case Figure 6 shows that the abundance deviations decrease somewhat. This is not only due to the resulting decrease in δ_{ini} , but also due to the dependence of dn/dM on collapse redshift. At higher z , dn/dM tends to favor lower mass scales where the abundance deviations are larger (Figure 5).

4.2.2. Fluctuations of Abundances Within Objects

The element abundances of collapsed objects can differ from primordial abundances in two ways. First, the abundances of an object could be uniformly different from the primordial values. This possibility was already discussed in the previous section. Second, if the element abundances within an object vary greatly from point to point, differences from the primordial abundances may be observed because of the fluctuations. We consider this latter effect by computing the standard deviation of the abundances within a given object. The lowest-order formula for this quantity is

$$\sigma_Y^2 = \bar{Y}^2 (1 - \bar{Y})^2 \sigma_{\Delta_Y}^2 \quad (44)$$

for ${}^4\text{He}$ and

$$\sigma_X^2 = \bar{X}^2 \sigma_{\Delta_X}^2 \quad (45)$$

for ${}^7\text{Li}$ and D. We have already calculated the mean values of the abundances, so now we only need the mean squares. We proceed as above, but this time we obtain a double integral that must be evaluated numerically,

$$\left(\Delta^2\right)_M = \frac{3}{8\pi^4 R^3} \int_0^\infty dk k \Delta_k \int_0^\infty dl l \Delta_l \left(\frac{\sin(k-l)R}{k-l} - \frac{\sin(k+l)R}{k+l} \right). \quad (46)$$

The integration region is the first quadrant of the $k-l$ plane. Since the integrand is symmetric with respect to the interchange of k and l , it is equal to the integral

$$\left(\Delta^2\right)_M = \frac{3}{4\pi^4 R^3} \int_0^\infty dk k \Delta_k \int_0^k dl l \Delta_l \left(\frac{\sin(k-l)R}{k-l} - \frac{\sin(k+l)R}{k+l} \right). \quad (47)$$

We carry out the integrations as with equation (41) and our results are plotted as a function of mass scale in Figure 7. Comparing Figures 5 and 7, we see that the relative importance of abundance fluctuations depends on the mass of the object in question. On small mass scales, abundances differ from their primordial values by an approximately uniform amount; but as the object size increases fluctuations from the mean are more likely to produce a difference from the primordial values. We also average the standard deviation over all collapsed objects in the Universe. Our prescription for this is identical to that given by equation (43), with σ_M taking the place of Y_M . These results are plotted versus the minimum mass scale for galaxies in Figure 8. Comparing this to Figure 6, we again see that the relative importance of fluctuations increases with increasing mass scale.

5. Observational Data

Though much recent work has focused on uncovering the primordial ${}^7\text{Li}$ and D abundances (e.g., Burles & Tytler 1998a,b; Tytler et al. 1999; Webb et al. 1997; Ryan et al. 2000), the ${}^4\text{He}$ abundance with a reported uncertainty of about 1%, is still more accurately determined. However, even this accuracy is at least an order of magnitude coarser than the mean effect of diffusion for low-mass objects. But, as discussed in § 4 the ${}^4\text{He}$ abundance is also expected to vary from point to point within an object. In this section, we re-examine the ${}^4\text{He}$ abundance data presented in Izotov & Thuan (1998) to determine whether or not such fluctuations are currently detectable.

In Izotov & Thuan (1998), the helium abundance is assumed to be linear in metallicity for low metallicity objects. Each data point consists of a measurement of the metallicity, Z_i , a measurement of the helium abundance Y_i , and estimations for the uncertainties in each, ϵ_i and δ_i . A straight line is fit to the data, the intercept of which reveals the primordial (zero-metallicity) helium abundance. The model we use is slightly different. Because of diffusion we cannot directly associate ${}^4\text{He}$ abundance measurements of zero-metallicity objects with the primordial ${}^4\text{He}$ abundance. Not only do we expect an object of a particular mass to have a ${}^4\text{He}$ abundance differing from the primordial value as shown in Figure 5, but also we expect that different measurements of the single object would display an intrinsic scatter about this mean as shown in Figure 7. Therefore, we fit the data to the following model. If an object has metallicity Z , the probability that it will have a ${}^4\text{He}$ mass fraction Y is denoted $g(Y|Z) dY$. We account for measurement uncertainties by defining $h(Y_i|Y)$ to be the probability of measuring Y_i if the object actually has abundance Y , and $f(Z|Z_i)$ to be the probability that an object has metallicity Z if Z_i is what is observed. Thus, the total probability of a measurement simultaneously obtaining Y_i and Z_i is

$$P(Y_i|Z_i) = \int f(Z|Z_i) g(Y|Z) h(Y_i|Y) dY dZ. \quad (48)$$

Both Z and Y are intrinsically positive, but we here assume that the uncertainties in the measurements are small enough so that the probability distributions f and h may be taken to be Gaussians,

$$f(Z|Z_i) = \frac{1}{\sqrt{2\pi\epsilon_i^2}} \exp\left[-\frac{(Z - Z_i)^2}{2\epsilon_i^2}\right], \quad (49)$$

$$h(Y_i|Y) = \frac{1}{\sqrt{2\pi\delta_i^2}} \exp\left[-\frac{(Y - Y_i)^2}{2\delta_i^2}\right]. \quad (50)$$

As for our model, we assume that

$$g(Y|Z) = \frac{1}{\sqrt{2\pi\sigma^2}} \exp\left[-\frac{(Y - mZ - b)^2}{2\sigma^2}\right]. \quad (51)$$

The parameters to be determined by the data are m , which contains the physics of the metallicity dependence; b , which is the mean value for the ${}^4\text{He}$ abundance; and σ , which represents the intrinsic scatter about the mean.

We use the integration in equation (48) to obtain

$$P(Y_i|Z_i) = \frac{1}{\sqrt{2\pi}} \frac{1}{\sqrt{\sigma^2 + m^2\epsilon_i^2 + \delta_i^2}} \exp\left[-\frac{(Y_i - mZ_i - b)^2}{2(\sigma^2 + m^2\epsilon_i^2 + \delta_i^2)}\right]. \quad (52)$$

If we determine the metallicity and helium abundance for N objects, the probability for the entire measurement to occur is

$$P_N = \prod_i^N P(Y_i|Z_i). \quad (53)$$

To maximize this probability with respect to the parameters m , b , and σ , we minimize the χ^2 -like function

$$\chi^2 = \sum_{i=1}^N \left[\ln(\sigma^2 + \delta_i^2 + m^2\epsilon_i^2) + \frac{(Y_i - mZ_i - b)^2}{\sigma^2 + m^2\epsilon_i^2 + \delta_i^2} \right]. \quad (54)$$

A downhill simplex method and a direction set method yielded almost identical parameters for the minimum χ^2 : $m = 4.8 \times 10^{-3}$, $b = 0.244$, and $\sigma = 1.52 \times 10^{-3}$. We used a Monte Carlo method to set confidence limits on these results. Because of random errors, the observed data points Z_i and Y_i are not a unique realization of the true values of the quantities. Instead, for a given measurement of Z_i , there are an infinite number of Y_i that could have been measured. The probabilities for obtaining these hypothetical measurements are assumed to be given by equation (52). We have generated 10^4 of these hypothetical data sets by substituting the observed values for m , b , and σ into equation (52). For each hypothetical data set, we again minimized equation (54) to obtain a new triplet of parameters m , b , and σ . Figure 9 shows the resulting intercepts b plotted against the scatters σ . The uncertainty in our best-fit sigma and intercept are large, and so the observational situation must improve before we could settle on the true parameters.

6. Conclusions

We have explored the effect of diffusion during the linear growth of density perturbations in the neutral IGM before the redshift of reionization and have found that element abundances within collapsed objects differ from their primordial values. Element diffusion leads to two related effects. First, the mean element abundances of a collapsed object could differ from the primordial values; and second, diffusion could result in abundance fluctuations within a single object. For objects with a total mass below $10^7 M_\odot$ the former effect dominates; but for larger objects the latter effect is more important. The magnitude of the effect is ~ 0.005 – 0.2% , depending on the mass of the object and the element. We have then used a Press-Schechter mass function to average these distributions over all collapsed objects in the Universe, and again found the net effect to be $< 0.1\%$. This effect is yet too small to be detected since the best observations of element abundances currently have accuracies of $\sim 1\%$.

If the effect of diffusion on element abundances will eventually be measured with sufficient precision in low-metallicity systems, the results could provide important clues about early struc-

ture formation in the IGM. In particular, the mean deviations within objects are sensitive to the minimum mass of a galaxy halo. Also, the overall magnitude of diffusion is sensitive to the redshift of reionization since diffusion is brought to a halt at that time. And as determinations of element abundances get more and more accurate, diffusion will eventually have to be accounted for in order to make comparisons with the predictions of big bang nucleosynthesis.

We thank Rennan Barkana for useful comments on the manuscript. This work was supported in part by NASA grants NAG 5-7039, 5-7768, and by NSF grants AST-9900877, AST-0071019.

REFERENCES

- Abel, T. 1995, Ph. D. thesis, Univ. Regensburg
- Barkana, R. 2000, private communication
- Barkana, R. & Loeb, A. 2001, *Physics Reports*, 349, 125
- Burgers, J. M. 1969, *Flow Equations for Composite Gases* (New York: Academic Press)
- Burles, S., Nollett, K. M., & Turner, M. S. 2001, *ApJ*, 552, L1
- Burles, S. & Tytler, D. 1998a, *ApJ*, 499, 699
- Burles, S. & Tytler, D. 1998b, *ApJ*, 507, 732
- Chiu, W. A., & Ostriker, J. P. 2000, *ApJ*, 534, 507
- Clementi, E., Raimondi, D. L., & Reinhardt, W. P. 1963, *J. Chem. Phys.*, 38, 2686
- Eisenstein, D. J. & Hu, W. 1999, *ApJ*, 511, 5
- Gnedin, N. Y. 2000, *ApJ*, 535, 530
- Gnedin, N. Y., & Ostriker, J. P. 1997, *ApJ*, 486, 581
- Haiman, Z., & Loeb, A. 1998, *ApJ*, 503, 505
- Haiman, Z., & Loeb, A. 1999a, in *AIP Conf. Proc.*, 470, *After the Dark Ages: When Galaxies Were Young*, Ninth Astrophysics Conf., College Park, MD, Eds. S. S. Holt, & E. P. Smith, 34
- Haiman, Z., & Loeb, A. 1999b, *ApJL*, 521, 9
- Izotov, Y. I., & Thuan, T. X. 1998, *ApJ*, 500, 188
- Loeb, A., & Barkana, R. 2001, *ARA& A*, 39, 19

- Massey, H. S. W., Burhop, E. H. S., & Gilbody, H. B. 1969, *Electronic and Ionic Impact Phenomena* (Oxford: Clarendon Press)
- Olive, K. A., Steigman, G., & Skillman, E. D. 1997, *ApJ*, 483, 788
- Pagel, B. E. J., Terlevich, R. J., & Melnick, J. 1986, *PASP*, 98, 1005
- Peebles, P. J. E. 1993, *Principles of Physical Cosmology* (Princeton: Princeton University Press)
- Peimbert, M., Peimbert, A., & Ruiz, M. T. 2000, *ApJ* 541, 688
- Peimbert, M., & Torres-Peimbert, S. 1974, *ApJ*, 193, 327
- Ryan S. G., et al. 2000, *ApJ*, 530, L57
- Schramm, D. N., & Turner, M. S. 1998, *Rev. Mod. Phys.*, 70, 303
- Seager, S., Sasselov, D. D., & Scott, D. 1999, *ApJ*, 523, L1
- Slater, J. C. 1964, *J. Chem. Phys.*, 39, 3199
- Spitzer, L. 1956, *Physics of Fully Ionized Gases* (New York: Interscience Publishers)
- Tegmark, M., Silk, J., Rees, M.J., Blanchard, A., Abel, T., & Palla, F. 1997, *ApJ*, 474, 1
- Tytler, D., et al. 1999, *AJ*, 117, 63
- Webb, J. K., et al. 1997, *Nature*, 388, 250

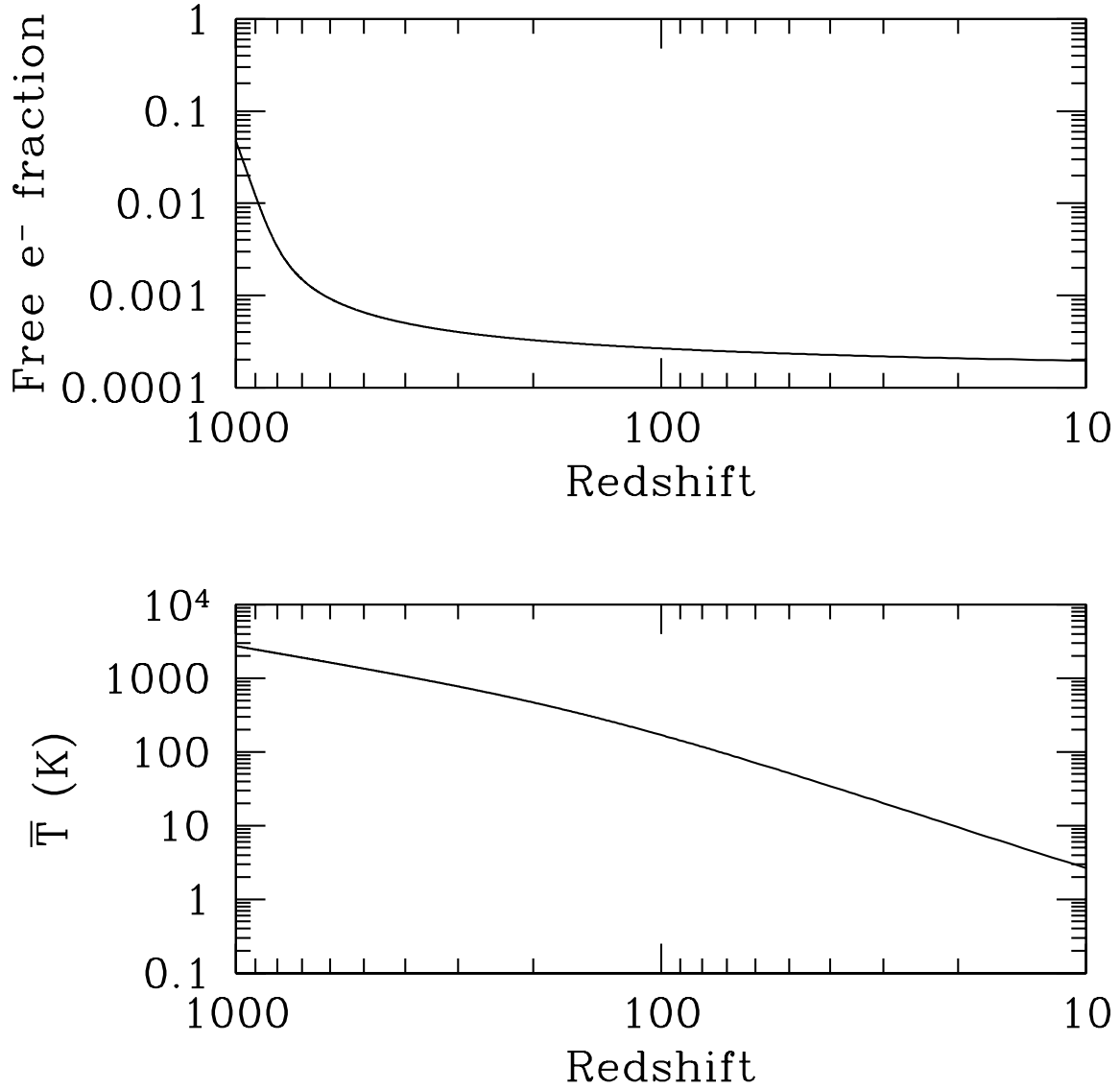


Fig. 1.— Top panel: The free electron fraction as a function of redshift. The Universe rapidly approaches neutrality after $z \approx 1000$. Bottom panel: The average baryon temperature as a function of redshift. For $z > 200$, the free electron fraction is still large enough so that the baryons are coupled to the background radiation, and so the baryonic temperature decreases like $(1+z)$. For smaller redshifts, the baryon temperature is mainly determined by the adiabatic expansion, and drops off like $(1+z)^2$.

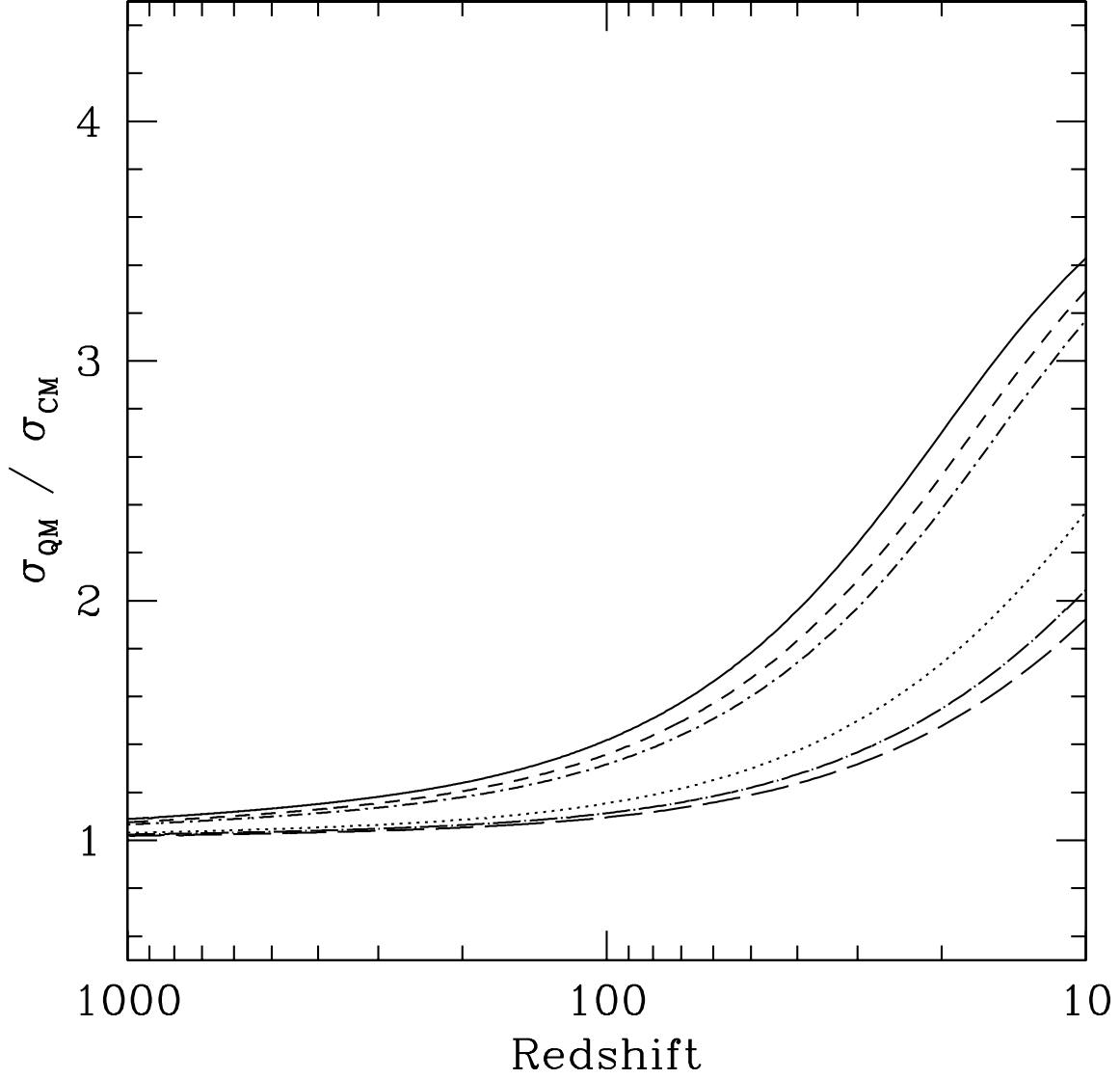


Fig. 2.— The inter-particle cross section, in units of the classical hard-sphere cross section. Solid line is $^1\text{H}-^4\text{He}$, dotted is $^1\text{H}-^7\text{Li}$, short dash is $^1\text{H}-\text{D}$, long dash is $^4\text{He}-^7\text{Li}$, dot-short dash is $^4\text{He}-\text{D}$, and dot-long dash is $^7\text{Li}-\text{D}$. This quantum-mechanical correction factor depends on the atomic radii, the reduced mass, and the temperature.

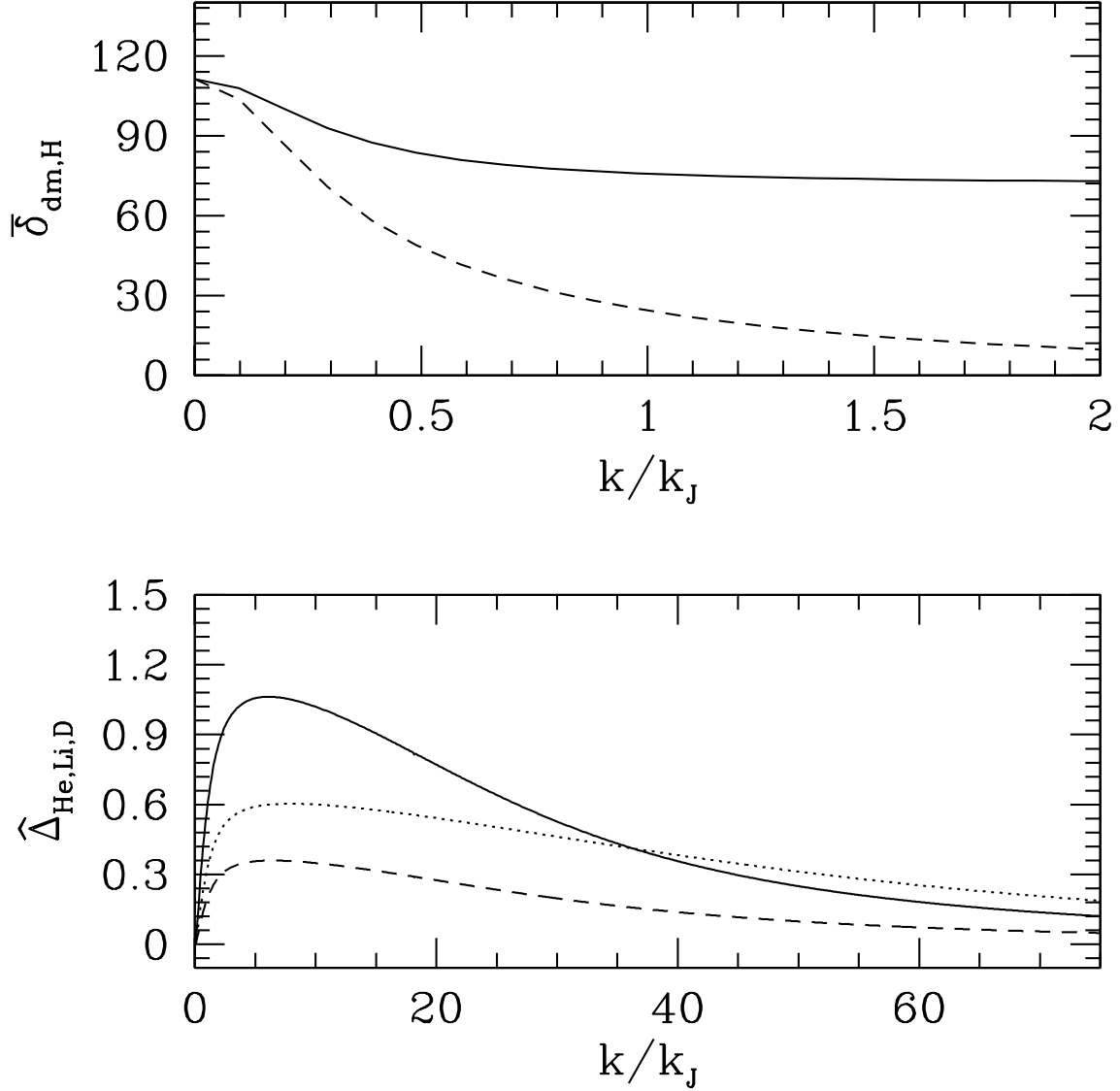


Fig. 3.— *Top panel:* The normalized dark matter (solid) and hydrogen (dashed) overdensities. For small k , both are amplified. But as k increases, pressure forces inhibit baryonic modes from growing. *Bottom panel:* The normalized differences relative to Hydrogen, $\hat{\Delta}_x$. The solid line has $x = {}^4\text{He}$, the dotted line has $x = {}^7\text{Li}$, and the dashed line has $x = \text{D}$. The relatively heavy mass and small atomic radius of ${}^4\text{He}$ make it particularly susceptible to diffusion.

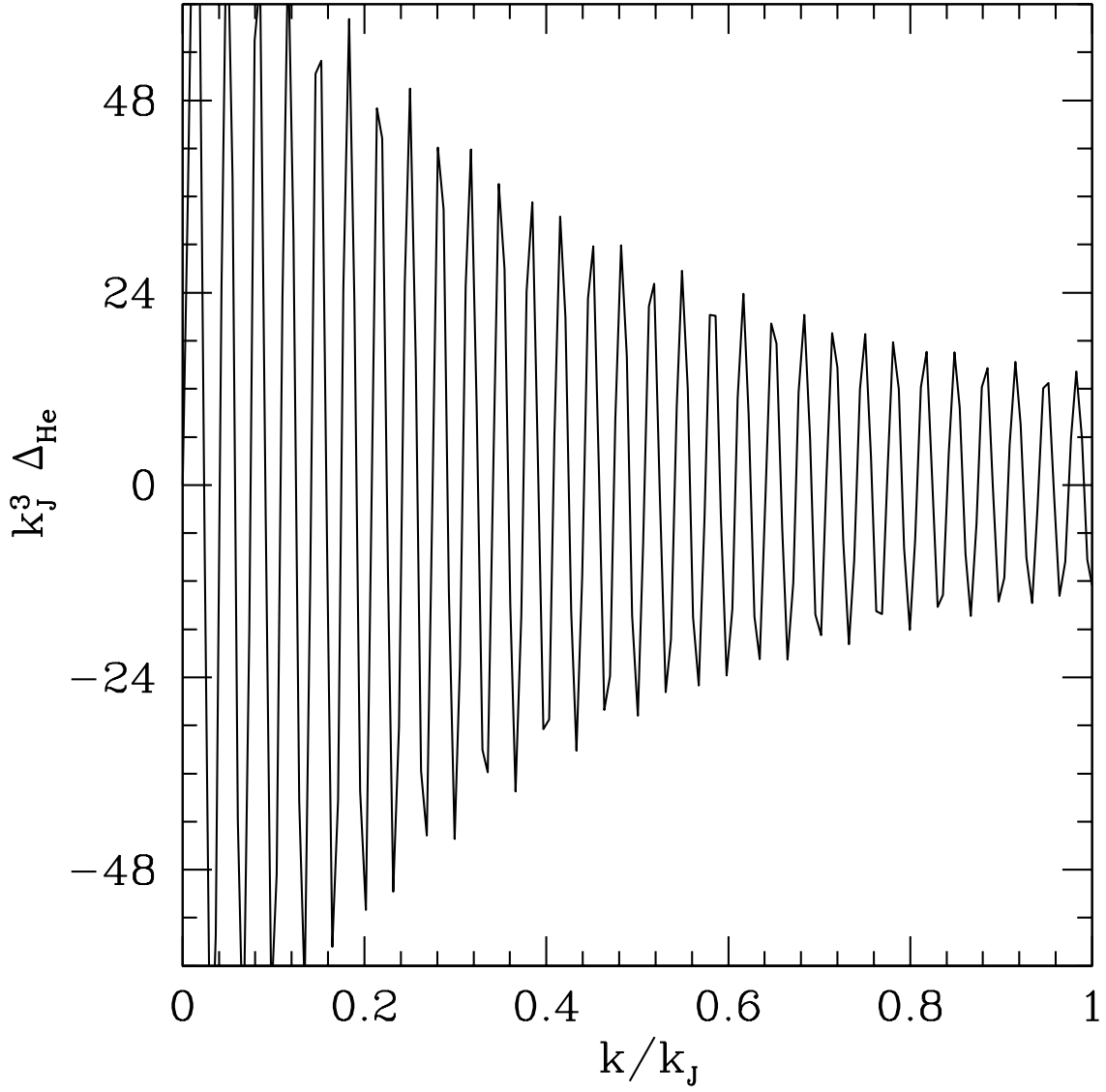


Fig. 4.— The difference Δ_{He} , for an overdense region with a mass of $10^9 M_\odot$. This plot is obtained by interpolating the smoothly varying normalized overdensities, and then multiplying each mode by its rapidly varying normalization factor.

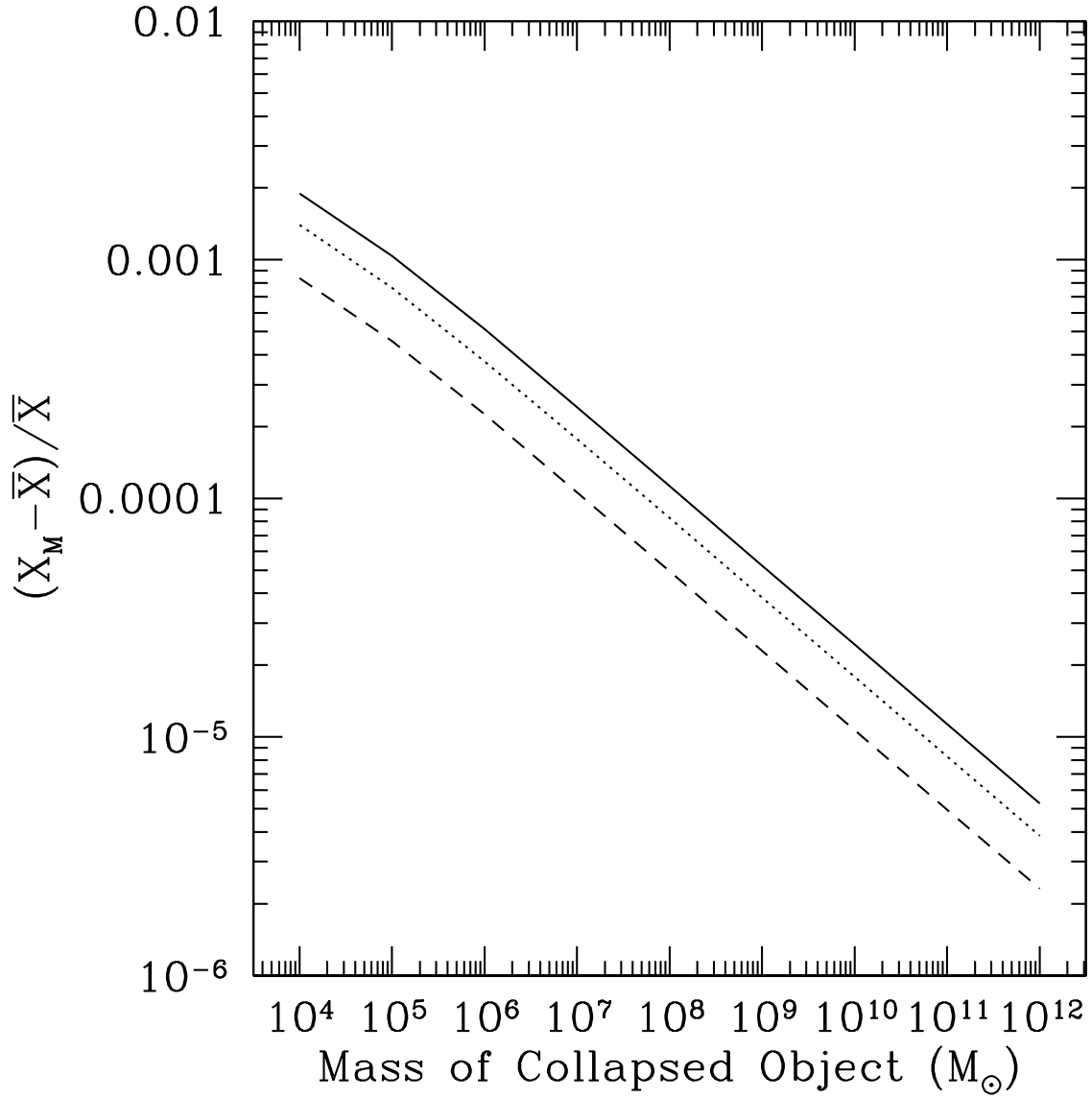


Fig. 5.— Fractional deviations from the primordial abundances for $z_{reion} = 8$. The solid line is the fractional deviation for ^4He , the dotted line is for ^7Li , and the dashed line is for D.

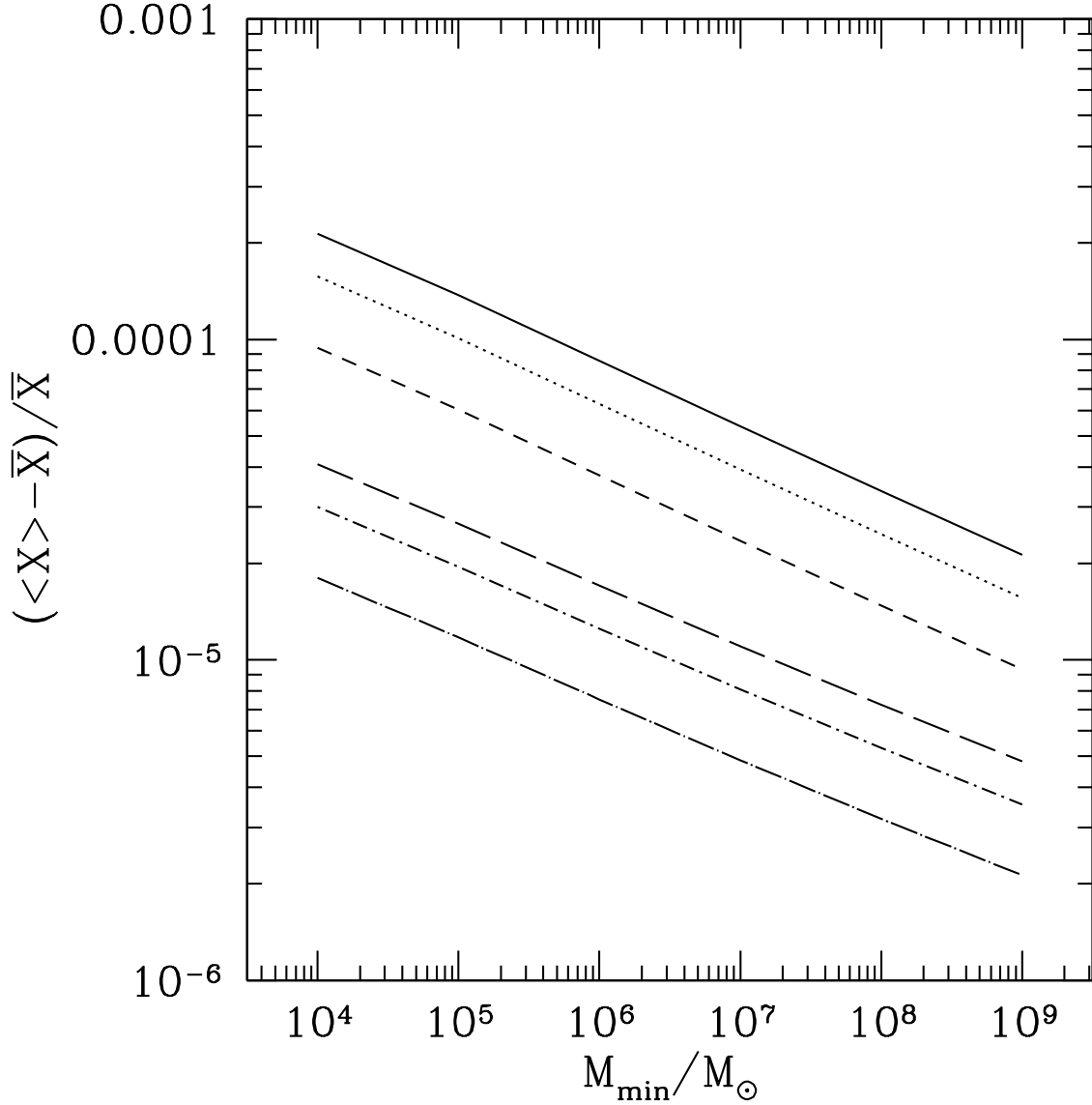


Fig. 6.— The fractional deviations averaged over all collapsed objects in the Universe, as a function of the minimum allowed mass scale for galaxies. We show two cases for the collapse redshift of the objects. For the first case with $z_{coll} = 2.5$, the solid line corresponds to the fractional deviation for ${}^4\text{He}$, the dotted line to ${}^7\text{Li}$, and the short-dashed line to D. For the second case with $z_{coll} = 0$, the long-dashed line corresponds to ${}^4\text{He}$, the dot-short dashed line to ${}^7\text{Li}$, and the dot-long dashed line to D.

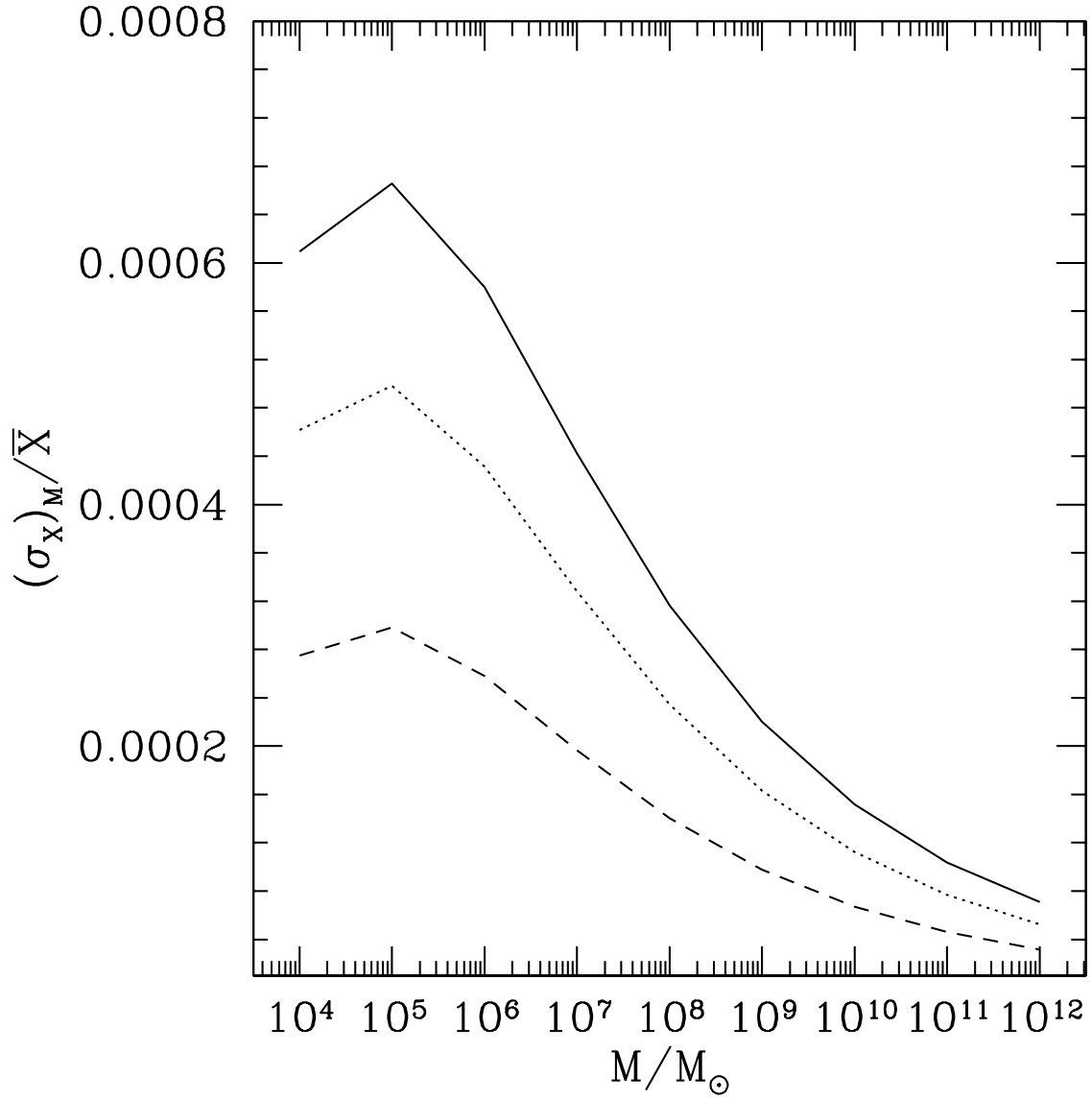


Fig. 7.— Standard deviations of abundances for $z_{reion} = 8$. The solid line is the standard deviation for ${}^4\text{He}$, the dotted line is for ${}^7\text{Li}$, and the short dashed line is for D.

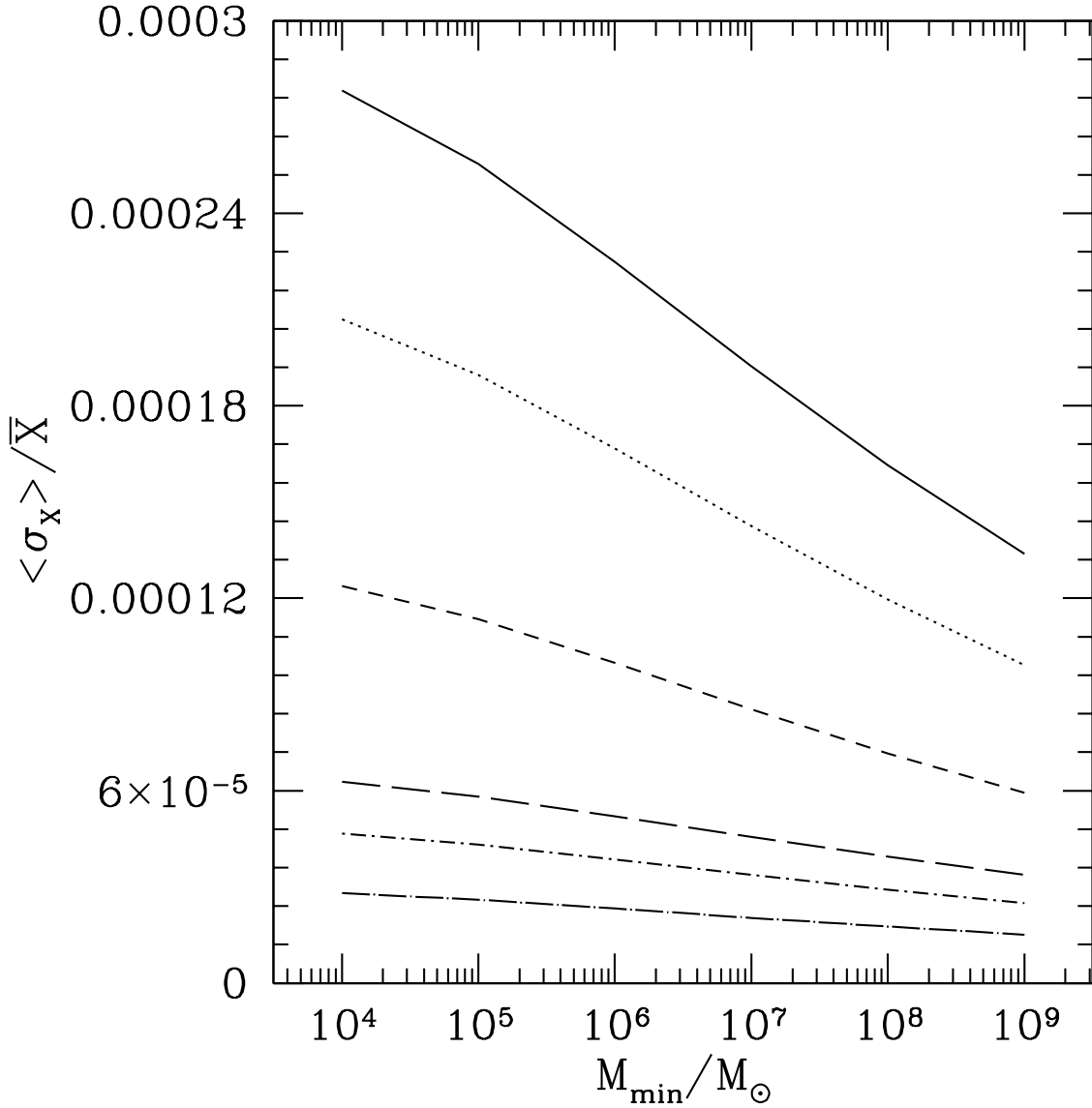


Fig. 8.— Standard deviations averaged over all collapsed objects in the Universe as a function of the minimum allowed mass scale. We show two cases for the collapse redshift: (i) $z_{coll} = 2.5$, for which the solid line is the standard deviation for ${}^4\text{He}$, the dotted line is for ${}^7\text{Li}$, and the short-dashed line is for D; (ii) $z_{coll} = 0$ for which the long-dashed line refers to ${}^4\text{He}$, the dot-short dashed line refers to ${}^7\text{Li}$, and the dot-long dashed line refers to D.

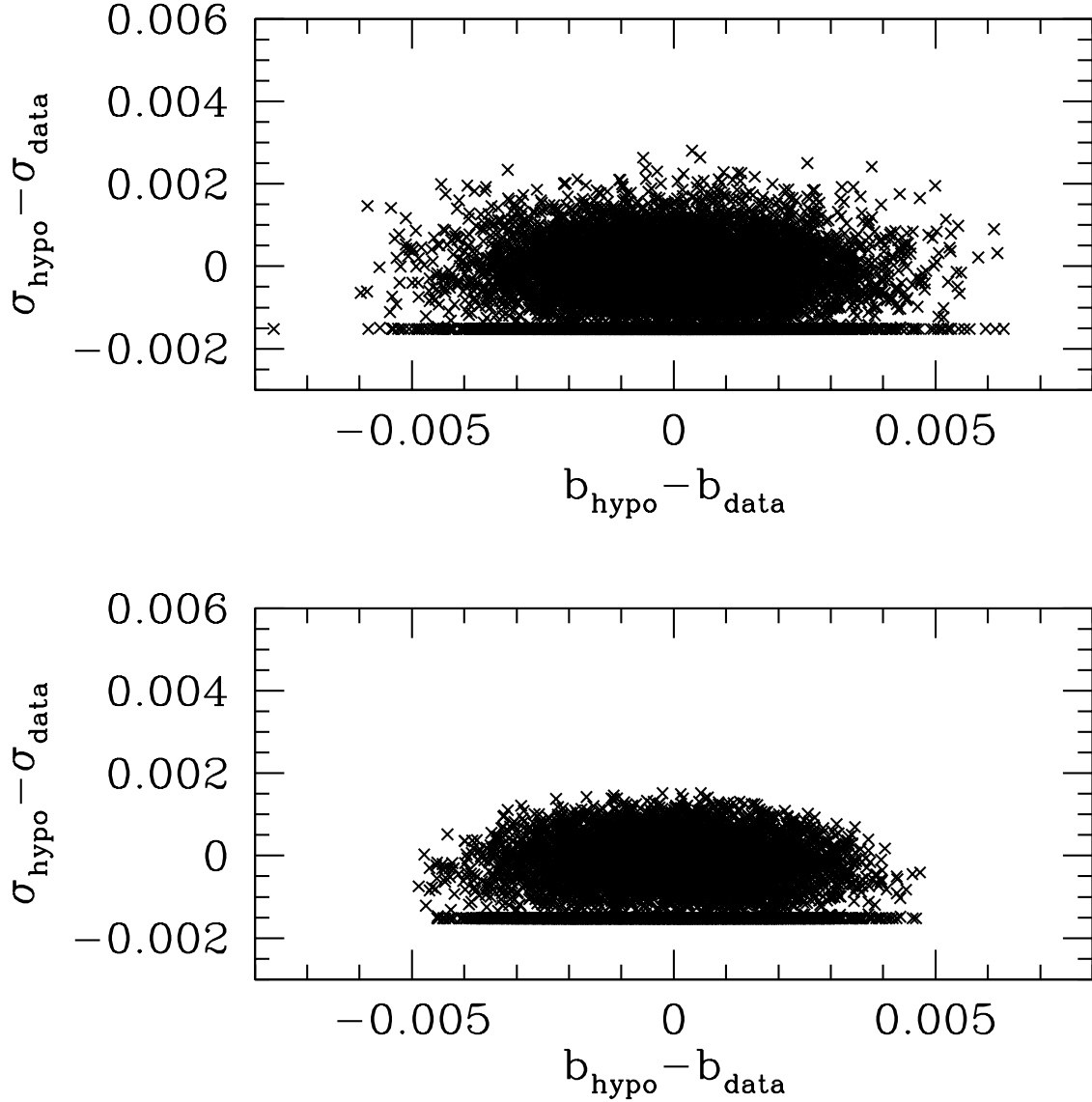


Fig. 9.— Results from 10^4 Monte Carlo data sets based on the model described in §5. The top panel shows all hypothetical $(b_{\text{hypo}}, \sigma_{\text{hypo}})$ pairs relative to the observed values $(b_{\text{data}}, m_{\text{data}})$, while the bottom panel show the 6,730 pairs most likely to occur. The extended horizontal concentration of points near -0.0015 occurs because of the physical constraint that all values of σ be greater than zero. This indicates that we have not yet reached the level of accuracy required to put a lower bound on σ .